What the Longest Exposures from the Hubble Space Telescope Will Reveal

JOHN N. BAHCALL, PURAGRA GUHATHAKURTA, DONALD P. SCHNEIDER

Detailed simulations are presented of the longest exposures on representative fields that will be obtained with the Hubble Space Telescope, as well as predictions for the numbers and types of objects that will be recorded with exposures of different durations. The Hubble Space Telescope will reveal the shapes, sizes, and content of faint, distant galaxies and could discover a new population of Galactic stars.

THE HUBBLE SPACE TELESCOPE (HST) IS SCHEDULED TO be launched soon and the first scientific observations should be available within several months. Many authors have discussed the qualitative advances that may be anticipated with an orbiting space telescope in such diverse areas as astrometry, interstellar matter, stellar evolution, galactic structure and evolution, quasar research, and cosmology (*1, 2*). For most observations, the HST will be pointed at individual objects or fields of special interest. We discuss the specific set of observations in which the telescope will take pictures of random fields (devoid of objects known a priori to be of special interest) in order to determine the statistical characteristics of faint galaxies and stars.

In this article we present quantitative predictions of what the HST images of these representative fields will show based upon what we know from ground-based telescopes. The comparison of the HST observations with these predictions will constitute an objective measure of what HST discovers about the properties of faint galaxies and stars. Our working hypothesis, which will be tested by HST observations, is that everything in the HST universe has previously been revealed by ground-based observations. Using this "parochial principle," we derive quantitative predictions for the numbers, colors, and types of faint galaxies and stars that will appear in the HST data. It will be especially exciting if HST observations reveal objects or structures not predicted in this article.

Our predictions for the total number of galaxies and of stars per square arc minute on the sky to various limiting brightnesses are shown in Table 1. It summarizes the calculated (cumulative) number of field galaxies and of Galactic stars that are present at high Galactic latitudes and are brighter than specified magnitude limits. The results in Table 1 can be used to estimate the expected number of objects that will be observed with different camera configurations aboard HST. The relative numbers of stars and galaxies per magnitude interval in our simulations are about equal at visual magnitude $V = 19.5$ (near-infrared magnitude $I \sim 18.5$); there are approximately 0.1 stars (or galaxies) arc min^{-2} mag^{-1} at this magnitude. By $V = 22.5$, the galaxies outnumber the stars by a factor of 10, and there are about 2.5 galaxies arc min^{-2} mag^{-1}. At $V = 25$, the expected number of stars ($\sim$0.35 arc min^{-2} mag^{-1}) is only 1% of the number of galaxies. The limiting flux level reached by long exposures on stars or faint, distant galaxies scales approximately proportional to the inverse square root of the observing time.

We do not expect HST to reveal a new population of galaxies. Ground-based observations can detect galaxies to a visual magnitude limit of about $V = 27$ (*3*). This is also the approximate detection limit for relatively compact objects (radius $\sim$0″.2) with HST in the longest planned exposures by guaranteed time observers (GTOs) (*4, 5*). For a given luminosity, the more compact the object the easier it is to detect. To escape detection from the ground but still be observed with HST, the faintest galaxies ($V > 27$) must have angular radii of less than $\sim$0″.2; this seems an unlikely possibility (see our discussion below of Fig. 4).

In agreement with previous authors, our analysis suggests that the major contribution of HST for galaxy research will be in revealing the shapes, sizes, and content of previously unresolved galaxies.

Table 1. The number density of faint galaxies and stars. The calculated total number of objects per square arc minute at high Galactic latitudes with visual magnitudes, V, and near-infrared magnitudes, I, less than the specified brightness, m. Also shown are the calculated number of stars per square arc minute. For specificity, the luminosity functions of faint spheroid and disk stars are assumed constant between $M_V = 12$ and $M_V = 16.5$ No brown dwarfs are included. The V galaxy counts are assumed to follow a power law beyond $V = 26$, and the I counts are V magnitude-limited with $V_{max} = 28$ and 30 for galaxies and stars, respectively. The numbers given here refer to the input data to the simulations and not to the numbers that would be detected, which depend upon exposure time, detector efficiency, background levels, and characteristics of the object identification code.

m	$N(<V)$ Total	$N(<V)$ Stars	$N(<I)$ Total	$N(<I)$ Stars
15	0.032	0.03	0.080	0.07
18	0.16	0.14	0.46	0.35
20	0.52	0.34	1.6	0.79
21	1.0	0.50	2.8	1.0
22	2.0	0.70	5.7	1.4
23	4.5	0.9	12.9	1.8
24	10.7	1.2	29.0	2.4
25	26.7	1.6	82.3	2.9
26	67.3	2.0	203	3.5
27	169	2.4	354	3.9
28	445	3.0	429	4.2
29	—	3.6	444	4.2
30	—	4.2	445	4.2

The authors are at the Institute for Advanced Study, Princeton, NJ 08540. J. N. Bahcall is also at the Space Telescope Science Institute, Baltimore, MD 21218.

Because of the high resolution of the telescope, HST should reveal important features of the brightness distributions of relatively compact galaxies, features that cannot be studied from the ground because of atmospheric blurring effects. Our principal assumption is that for the faintest galaxies the average size as a function of brightness lies within the range indicated by existing ground-based observations. We show in what follows that those HST images that reach to faint magnitudes should test the validity of this assumption.

In contrast to the situation for galaxies, HST observations should provide a qualitative increase in our knowledge of populations of faint stars. HST observations should determine the relative numbers of faint, low-mass main sequence stars of different brightnesses, a task that has proved very difficult with ground-based observations.

The space images may also provide a more spectacular breakthrough. Many authors have suggested that the "missing" matter in the disk or halo of our Galaxy is composed of faint stars, usually called brown dwarfs, that are not massive enough ($M < 0.08\ M_\odot$) to fuse hydrogen. If the missing mass is in the form of brown dwarfs, deep HST images may reveal this new population of stars by a characteristic increase in the number of observable stars by a factor of 4 for each magnitude fainter that the image reaches (*6*); this contrasts with the slow increase in the number of normal stars at faintness limits obtainable from the ground (*7*). Images obtained with ground-based telescopes cannot identify stars at sufficiently faint magnitudes to detect many brown dwarfs at their expected brightnesses. For visual magnitudes much fainter than 21, it is difficult to separate stars from galaxies by means of ground-based observations and the number of galaxies greatly exceeds the number of stars, further complicating the analysis of ground-based data. As many as 100 brown dwarfs could appear on a picture taken with HST's Wide Field Camera (WFC) (*4*) that extended to an infrared magnitude of $I = 26$ (25 of them having $I < 25$) if the missing mass in the Galactic halo is composed entirely of brown dwarfs. This discovery would imply, contrary to some theoretical ideas (*8–9*), that the majority of the halo brown dwarfs have not yet cooled beyond the limiting sensitivity of HST. For the simplest case in which all of the brown dwarfs have the same absolute luminosity and mass, the number with an apparent infrared magnitude ($m_{\rm IR}$) brighter than I is:

$$n(m_{\rm IR} \leq I) = 100\left(\frac{\rho}{0.01\ M_\odot\ {\rm pc}^{-3}}\right)\left(\frac{0.08\ M_\odot}{M_{\rm brown\ dwarf}}\right) \times 10^{0.6[(I\ -\ 26)\ -\ (M_I\ -\ 15)]} \quad (1)$$

for the area of a WFC field (7.1 arc min^2). Here ρ is the halo density in the form of brown dwarfs in solar masses per cubic parsec and M_I is the absolute I band magnitude of the brown dwarfs. Possible values of these quantities are also indicated: $\rho_{\rm halo} \sim 0.01\ M_\odot\ {\rm pc}^{-3}$ (*7*), $I_{\rm limiting} \sim 26$ (a conservative limit for a moderately long exposure), and $M_I \gtrsim 15$ (the greatest source of uncertainty). The number of brown dwarfs in the disk could be of order ten or so per deep WFC field if the missing matter in the disk is all brown dwarfs. Some of these objects may be young enough to appear on deep WFC images. Brown dwarfs will be visible either by the rapid increase in the total star counts due to the appearance of the new population (see the $10^{0.6I}$ factor in Eq. 1) or by the discovery of very red objects with $V - I > 4$.

The longest HST exposures will also provide important new information on the number of faint quasi-stellar objects, quasars. The most accurate ground-based determinations of quasar numbers (*10*) do not reach fainter than blue magnitude $B = 21$, a limit which could be extended by a factor of more than a thousand in brightness by HST images. A naive extrapolation of the ground-based observations would suggest that the quasar number density at faint magnitudes could be of order $3 \times 10^{0.3(V\ -\ 29)}$ per square arc minute (assuming $B - V \sim 0$), which is comparable to the estimated number of faint Galactic stars (see Table 1). This extrapolation must break down within the range of brightnesses accessible to HST because of the absorption by intervening material of the light emitted by intrinsically bright and distant quasars. The nuclei of Seyfert galaxies (quasar-like, but intrinsically fainter) can be seen by HST to redshifts of order four and perhaps beyond, greatly extending our knowledge of their evolution.

We have made simulations of what the WFC will record because this camera has the largest field of view of any imaging detector on HST and is also the most sensitive in the color range we are investigating. The WFC's field of view is 160″ by 160″—a mosaic of four 800 by 800 Charge-Coupled Devices (CCDs) with 0″.1 pixels. The Faint Object Camera (FOC) (*5*) has a much smaller field of view, 22″.5 by 22″.5, in its broadest imaging mode. The number of objects expected for the FOC, to a given limiting magnitude, can be obtained by dividing the WFC numbers by 50.

Our results show that moderately long (typical usable portion of one orbit = 2300 seconds) exposures in the visual band with the WFC are expected to reveal relatively few objects, only of order 150 galaxies and 20 stars. The longer exposures may be much richer in galaxies, although perhaps not in stars. The simulations suggest that the the longest planned observations by the GTOs, 11 co-added orbits, will yield somewhere between 400 and 1700 galaxies and about 30 stars. The greatest recognized uncertainties in these predictions are caused by the extrapolation of the observed dependence of the average galaxy size upon faintness and the estimation of the effects of crowding in the ground-based images fainter than $V \sim 26$.

For the simulations presented in this article, we have used properties of galaxies and of stars that are known from ground-based photometric optical imaging. In order to estimate certain galaxy parameters, we have been forced to extrapolate quantities that have been measured accurately only for relatively bright galaxies ($V \lesssim 15$), even though the vast majority of galaxies in the simulated images (and those expected to be detected in the WFC deep images) are much fainter ($V > 22$).

Our results show that the most sensitive exposures achieved so far from the ground reveal more galaxies per unit area than will be seen by planned HST observations unless galaxy sizes decrease with apparent brightness at the maximum rate consistent with existing ground-based observations. In this, the most favorable case for HST, the space exposures will show almost as many galaxy images as have been observed so far in the most sensitive ground-based data.

Figure 1 is constructed with simulation software (*11*) that embodies the characteristics of the HST, the WFC, and the expected number density of galaxies and stars as a function of apparent magnitude. Each frame represents one quarter of a WFC field (80″ by 80″). These pictures are in some sense "ideal" images; the effects of cosmic rays and detector systematics are presumed to be removed perfectly from the images.

A simulation of a moderately long exposure, one orbit or 2300 seconds, made with the wide band visual (V) filter (F555W) is shown in Fig. 1A. This simulation suggests that HST images of high-latitude random fields will not contain many objects unless extremely long exposures are taken.

Our best estimates of what will be observed on very long exposures in which data from eleven orbits are co-added are shown in Fig. 1, B and C. Figure 1B simulates observations made with the wide band visual filter (same as for Fig. 1A except that the exposure time is 11 times longer) and Fig. 1C simulates observations made with the broad band I filter (F785LP). The simulations refer to the longest broad band observations (slightly more than 7 hours) on a single field by the HST GTOs (*2*). The much larger number of objects in Fig. 1, B and C, than in Fig. 1A shows how important long exposures are expected to be for this HST program.

In Fig. 1D a simulation is shown for the same observing setup as Fig. 1B except that the angular size-magnitude relation for galaxies is assumed to have the maximum steepness consistent with ground-based data (see the steep case described by Eq. 4). The smaller angular size of the galaxies in this simulation results in a much larger number of "detections."

The four brightest galaxies in each of the V simulations can be recognized as spiral galaxies with $22 < V < 23$. Among the next five galaxies ordered in brightness ($23.0 < V \leq 23.4$), two are ellipticals and three spirals. The six brightest I galaxies have $I < 22$ (five spirals and one elliptical). The stars visible in the simulated long V exposures, Fig. 1, B and D, have visual magnitudes of $V = 24.0$, 25.3, 26.0, 26.2, 26.3, and 27.4 (two stars). Of these seven stars, the five brightest are easily detectable in the one orbit V simulations (Fig. 1A). The stars visible on the long I simulation, Fig. 1C, are distributed as follows: $23 < I < 24$ (six stars), $24 < I < 25$ (two stars), and $I \sim 27$ (two stars). The brightest eight stars are detectable in a simulated moderately long (one orbit) I exposure. There are relatively few observable stars in the small area of our simulated images and their brightness distribution is severely affected by small number statistics. Tests with the automated object detection and analysis software package FOCAS (*12*) show that the stellar 50% detection limits are $V \sim 29.0$ and $I \sim 27.5$ for 11 co-added orbits. Further optimization of the detection filters should push these limits slightly deeper.

The FOCAS software has also been used to identify objects in the 800 by 800 pixel (a quarter of a WFC field) simulated images of Fig. 1, as well as in a number of other hypothetical observations. In the simulation of the one orbit observation, Fig. 1A, the object detection software found 34 galaxies and five stars. For Fig. 1, B and D (the two long V images), the automatic software found 138 and 425 objects, respectively; the 50% incompleteness limits for galaxies are $V \sim 26$ (Fig. 1B) and 27 (Fig. 1D). For Fig. 1C, FOCAS detects 157 objects; the corresponding 50% incompleteness limit is $I \sim 25$. Note that the detection limits refer to total apparent magnitudes for the galaxies. At the detection thresholds, the isophotal magnitudes are significantly fainter, since only the brightest central part of the galaxies stand up above the background. The morphological properties of the faintest galaxies (compare Eqs. 2

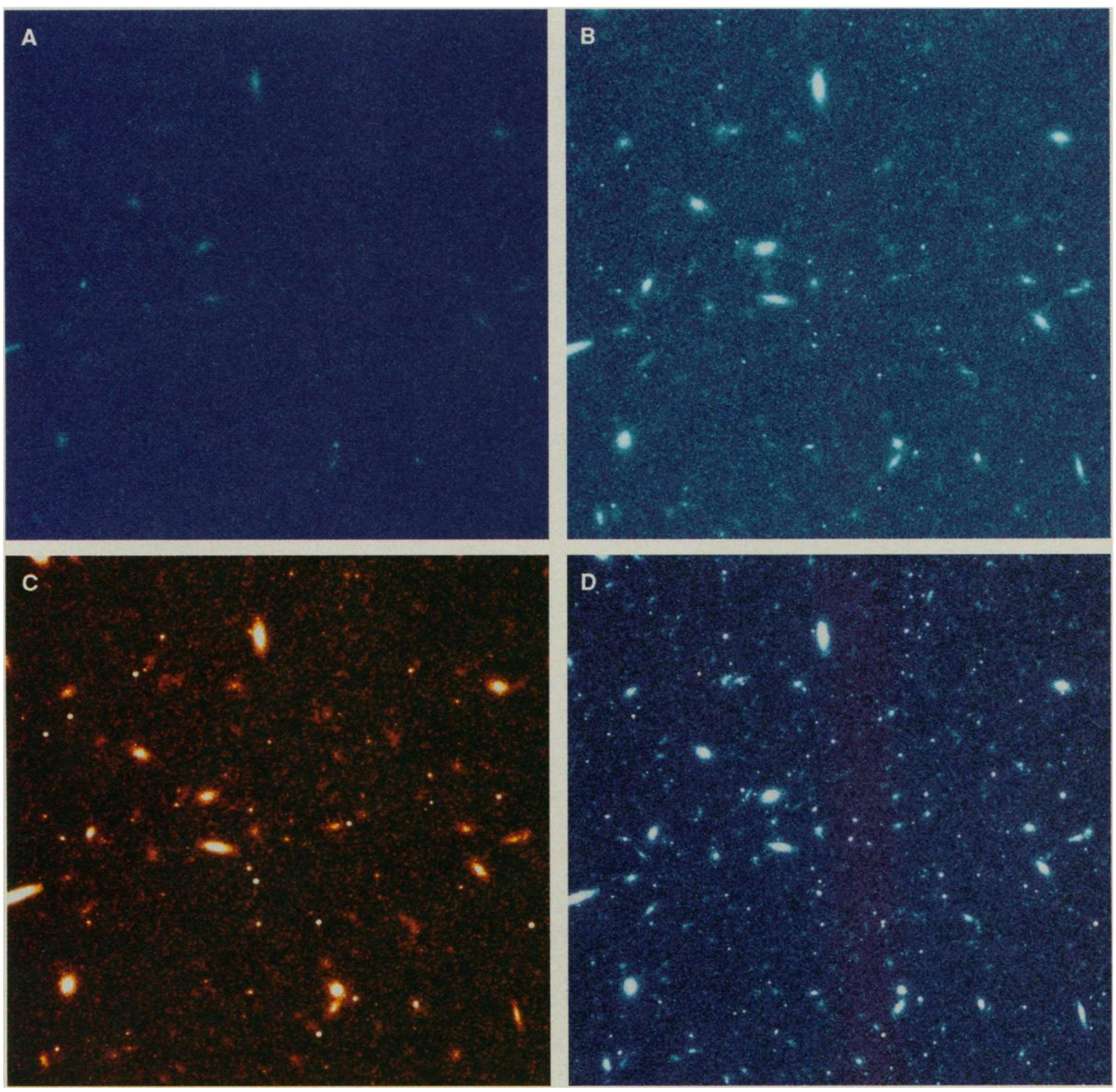

Fig. 1. (**A**) Simulated HST image in a visual broad filter, F555W, taken for one orbit (2300 seconds). The simulation shows what may be observed with HST at high Galactic latitudes in an 800 by 800 pixel image with the WFC, one quarter of the total WFC field, after the removal of cosmic ray events. The best estimate or normal extrapolation of the dependence of galaxy size upon faintness (see Eq. 2) was used in the simulation. A total of 34 galaxies and five stars were detected in our simulations of one quarter of the WFC field. (**B**) Simulated 11-orbit HST image in F555W. Same as (A) except that the exposure time was assumed to be for 11 co-added orbits. A total of 131 galaxies and seven stars were detected in our simulations of one quarter of the WFC field. (**C**) Same as (B) except that the picture was assumed to be taken through an infrared filter F785LP. A total of 147 galaxies and ten stars were detected in our simulation of one quarter of the WFC field. (**D**) Steep extrapolation: Simulated HST image in F555W co-added for 11 orbits. Same as (B) except that the steep extrapolation of the dependence of galaxy size upon faintness (see Eq. 4) was used in the simulation. A total of 418 galaxies and seven stars were detected in our simulations of one quarter of the WFC field.

and 4) will be important in determining the detection thresholds for actual WFC images.

Ground-based multiband photometry of field galaxies reveals evidence for luminosity and color evolution in these systems at apparent blue magnitudes fainter than about $B_J = 23$ or $V = 22.5$ (*3, 13*). It may be expected, therefore, that the appearance of these galaxies will change as they get intrinsically brighter and bluer with increasing look-back time. In the absence of morphological information for evolving faint galaxies, we have extrapolated to HST sensitivity and resolution by assuming no structural evolution; this hypothesis will be tested quantitatively (and presumably modified) by deep HST images.

Stars

The distribution of stellar V magnitudes was calculated with the widely circulated computer code embodying the Bahcall-Soneira Galaxy model (7). This model galaxy contains a thin disk and an older population of spheroidal stars, and describes well the observed distribution of stars in the Galaxy in different directions, colors, and magnitudes, for $6 < V < 21$, the range of magnitudes for which systematic ground-based observations are possible. For specificity in the predictions, we have assumed that the luminosity functions of faint spheroid and disk stars are constant between $M_V = 12$ and $M_V = 16.5$ [compare with figure 12 of (7)]. This assumption will be tested and corrected by HST observations.

At the apparent magnitudes of interest here, the majority of the stars in the model at high Galactic latitudes are on the main sequence (only 3% are giants). About 82% of all stars with $V < 30$ belong to the spheroid, the remainder are disk stars. At brighter magnitudes, the disk population constitutes a higher fraction of the stars (for example, of all stars with $V < 27$, about 30% are disk stars; this fraction rises to 50% for a limiting V magnitude of 20). Most of the faint stars in the model at high latitudes are from the spheroid population; disk stars dominate at brighter magnitudes ($V < 20$). Of course, disk stars dominate at low Galactic latitudes.

The magnitude and color dependences of the stellar components of the galaxy model are illustrated in Fig. 2. The predicted distribution of stellar $B - V$ colors is shown for four different apparent magnitude bins: (i) $V < 20$ (Fig. 2A), (ii) $20 \leq V < 25$ (Fig. 2B), (iii) $25 \leq V < 27$ (Fig. 2C), and (iv) $27 \leq V < 30$ (Fig. 2D). In each case, the thin solid line and the dashed line represent disk and spheroid stars, respectively, while the bold solid line shows their sum (that is, all stars in the given magnitude range, normalized to unity). The color distribution displays two distinct peaks at $B - V \sim 0.5$ and 1.5. The blue population consists of relatively bright ($V \lesssim 20$), mostly spheroid stars, while the majority of stars with $V > 23$ belong to the redder category. The Bahcall-Soneira galaxy model predicts about 30 stars per WFC field at high Galactic latitudes down to a limiting magnitude of $V = 30$.

The stellar I magnitudes were calculated by starting with all stars with $V < 30$, and assigning $V - I$ colors based on the stellar $B - V$ colors and the color-color relation of Johnson (*14*). Thus the

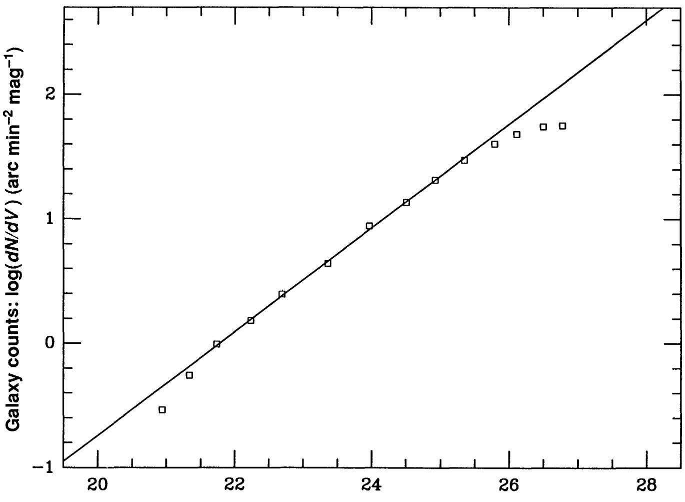

Fig. 3. Differential galaxy counts, $\log(dN/dm)$ in the V band. The open squares are the counts obtained from crowding corrected deep B_J counts (*3*) transformed to the V band with the use of $B_J - R$ colors (*15*). The solid line is a single power-law approximation: $\log(dN/dV) = 0.417\ V - 9.08$.

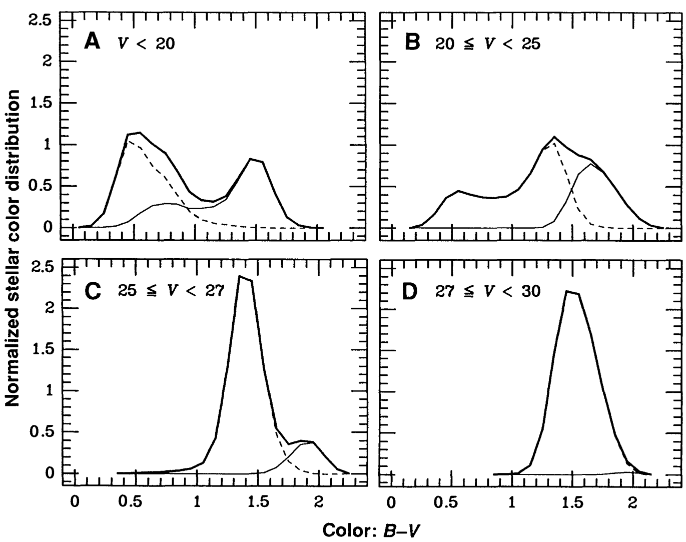

Fig. 2. The stellar $B - V$ color distribution from the Bahcall-Soneira galaxy model (7) for the apparent magnitude ranges: (**A**) $V < 20$; (**B**) $20 \leq V < 25$; (**C**) $25 \leq V < 27$; and (**D**) $27 \leq V < 30$. The thin solid and dashed lines show disk and spheroid stars, respectively, and the bold solid line (normalized to unity) represents their sum.

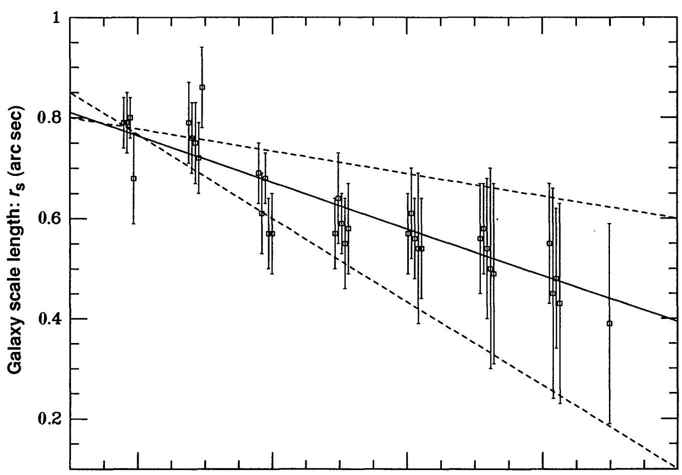

Fig. 4. Galaxy scale length r_s as a function of apparent V magnitude. The open squares are from Tyson and Wenk (*17*). Each square represents all of the galaxies in a given field within the appropriate V magnitude interval, and the error bar is the 1σ uncertainty in r_s. The solid line is an approximate fit, and the dashed lines indicate extreme relations that are marginally consistent with the observations.

simulated stars are V magnitude-limited with $V_{max} = 30$. An approximate calculation shows that the fact that the simulated stars are selected in V causes an error of less than 10% in the total number of stars predicted in the I band, unless there is a large previously undiscovered population of faint red stars ($V - I > 3.5$).

Galaxies

The expected number of galaxies was calculated as a function of apparent V magnitude with the use of the results of ground-based observations of field galaxies with CCD detectors. We used the blue (B_J) counts presented by Tyson (*3*) together with the $B_J - R$ versus B_J color-magnitude relation for faint galaxies (*15*) and the color transformation equations given by Gullixson *et al.* (*16*).

The V counts are shown as open squares in Fig. 3. The crowding of galaxy images in the ground-based data constitutes the main uncertainty, apart from morphological considerations, in deriving the expected galaxy counts. The ground-based galaxy counts show an apparent turnover attributable to the effects of crowding (the difficulty of identifying individual objects when images are crowded close to one another) at $B_J \sim 25$–26, about two magnitudes brighter than the faintest detectable galaxies in the Tyson (*3*) CCD data. Tyson has corrected the counts for crowding by testing the detection efficiency of the software at various apparent magnitudes. The counts shown in Fig. 3 are based on corrected counts, which we represent with a single power law approximation (solid line). At the bright end, the count slope must approach the Euclidean value of 0.6, but there are few galaxies in our simulations at these magnitudes. The apparent flattening of the counts at $V \sim 26$ is partly due to color selection bias in $B_J - R$ and partly due to a flattening in the corrected B_J counts. However, the latter takes place at an apparent magnitude where the crowding corrections are large, and we have assumed the power law to be valid beyond $V = 26$. The great resolution of the HST will obviate the need for significant crowding corrections at the magnitude limits discussed here (compare the panels in Fig. 1).

Most galaxies observed from the ground with $B_J < 26$ have angular profiles that are significantly broader than the seeing Point Spread Function (PSF) (*3, 17*). By co-adding individual galaxy images in different apparent magnitude intervals, and fitting the resulting surface brightness profiles to exponentials $[I(r) = I_0 \exp(-r/r_s)]$ convolved with the PSF, Tyson and Wenk (*17*) derive angular scale lengths r_s as a function of B_J. We have transformed the B_J magnitudes to V as described earlier for the number counts, assuming that the scale length of each galaxy is independent of the wavelength at which the measurement is made.

The open squares in Fig. 4 show the preliminary r_s versus V relation derived from five of the fields studied by Tyson (*3*) and Tyson and Wenk (*17*). The solid line in Fig. 4 represents

$$r_s = -0.046\ V + 1.69 \quad \text{(normal)} \tag{2}$$

with r_s in arc sec. We have also investigated the implications of two possible extreme $r_s - V$ relations that are marginally consistent with the data,

$$r_s = -0.022\ V + 1.22 \quad \text{(flat)} \tag{3}$$

and

$$r_s = -0.083\ V + 2.43 \quad \text{(steep)} \tag{4}$$

which are indicated by the dotted lines in Fig. 4. The exact form of the extrapolation of the scale length with apparent magnitude (Eq. 2, 3, or 4) represents the main uncertainty we can identify at this time in predicting the expected number of galaxies that will be detected by the HST in a given exposure time. For a galaxy of given apparent magnitude, the smaller the scale length, the greater will be its central surface brightness, thus making it easier to detect. HST observations will provide much more accurate measures of r_s than is possible with ground-based data.

To construct an accurate simulation, we also need to know the distribution of axis ratios (ellipticities) of galaxies. Our simulation is based on the axis ratio distribution of an angular-diameter-limited sample of 3421 UGC galaxies with Zwicky magnitudes less than 15 (*18*). We have adopted an analytic approximation, $f(r)$, to the normalized probability distribution of axis ratios obtained for the UGC catalog galaxies of

$$f(r) = 3.78r \exp(-r) \tag{5}$$

where the axis ratio, r, varies between zero and one. The morphological classification listed in the UGC catalog has been used to divide the sample into: (i) early types (including galaxies of type E, S0, SB0, E/S0, S0/a, and SB0/a), and (ii) late type galaxies (all other Hubble types). As a function of the axis ratio we adopt the following analytic approximation, $g(r)$, to the observed ratio of early to late type galaxies:

$$\begin{aligned} g(r) &= 0.58r && (r < 0.48) \\ &= 1.41r - 0.40 && (0.48 \le r < 0.75) \\ &= 0.66 && (r \ge 0.75) \end{aligned} \tag{6}$$

The shapes of both $f(r)$ and $g(r)$ are approximately independent of magnitude within the UGC catalog for magnitudes that are not affected by incompleteness (Zwicky mag $\lesssim 15$). We have ignored the fact that the UGC axis ratios may be subject to observational selection effects, since the results in this article are not very sensitive to the choice of $f(r)$.

To determine the galaxy magnitudes in the simulated I band image, we have followed the same procedure as was used for the stars—that is, we started with the V magnitude and assigned a $V - I$ color to each galaxy based on ground-based color data. The scale length r_s, the isophotal axis ratio r, and morphological type for each object is taken to be the same in V and I. From ground-based data on the faint field galaxies in question, one does not know the color distributions of late and early type galaxies separately. In the absence of this information, the $V - I$ color assigned to a galaxy is based on the observed color distribution of all galaxies, and the Hubble type of the particular galaxy is ignored. Thus comparisions of galaxy colors between the HST images and our simulations should be made without reference to any morphological parameters.

The Guhathakurta (*15*) $B_J - R$ data and synthesized $R - I'$ have been combined to produce $V - I$ colors for the simulated galaxies. It is necessary to use synthesized colors since ground-based I' data do not go very deep, resulting in severe color selection bias in $R - I'$ for $R \gtrsim 25$. Tyson (*3*) applied a statistical correction to the mean $R - I'$ to account for this bias, and our colors are synthesized to be in agreement with his. Note that we have extrapolated our fit to the $R - I'$ colors beyond $I \sim 24.5$. The I detection threshold for galaxies is not much fainter than this, although its exact value depends on how the scale length r_s changes with magnitude. The derived mean $V - I$ colors run from about 1.3 at the bright end ($V \sim 20$) to ~ 0.9 for $V \gtrsim 24$, and the 1σ spread varies from 0.3 to 0.6 mag.

Conclusion

Observations within the first year of operation of HST should confirm or reject the quantitative understanding exemplified by the simulations shown in Fig. 1 and by the general predictions embodied in Table 1. Significant departures from these expectations would indicate that there are new populations of astronomical objects or that previously identified populations have evolved in unexpected ways. In particular, the presence or absence of large numbers of brown dwarfs (Eq. 1) should be obvious from an analysis of the first deep scientific exposures with the WFC.

The HST project is developing the capability for operating instruments in a "parallel" mode, a mode in which one could, for example, take an exposure with the WFC in whatever direction it is oriented while another instrument is taking data on a specific object or field in a pointed mode. The typical length of time that the HST will be pointed at a particular target is about 20 minutes. The calculations presented in this article suggest that at high Galactic latitudes one may expect to detect in 20 minutes, with the WFC and a broad band visual filter, of order 100 galaxies and 20 stars over the entire WFC field. In the ultraviolet, a smaller number of objects are expected to be detected because galaxies, and particularly faint stars, have spectral energy distributions that decrease toward shorter wavelengths and the sensitivity of the WFC is much less in the ultraviolet than in the visual. The number of detected objects expected for different exposure times can be estimated from Table 1 and the fact that the limiting brightness that can be observed depends (for longer exposures) on approximately the square root of the observing time. The number of objects to a given magnitude that will be detected by the FOC is reduced by a factor of 50 compared to the WFC because of the smaller observing area; the FOC quantum efficiency peaks in the ultraviolet (but is never as large as the visual band efficiency of the WFC).

REFERENCES AND NOTES

1. D. N. B. Hall, Ed., *The Space Telescope Observatory* (NASA Scientific and Technical Information Branch, Washington, DC, 1982); L. Spitzer, *Science* **161**, 225 (1968).
2. M. S. Longair and J. W. Warner, Eds., *Scientific Research with the Space Telescope*, IAU Colloquium 54, NASA CP-2111 (U.S. Government Printing Office, Washington, DC, 1980).
3. J. A. Tyson, *Astron. J.* **96**, 1 (1988).
4. J. Westphal, in (*1*), p. 28.
5. F. Machetto, in (*1*), p. 40.
6. J. N. Bahcall and R. M. Soniera, *Astrophys. J. Suppl.* **47**, 357 (1981).
7. J. N. Bahcall, *Annu. Rev. Astron. Astrophys.* **24**, 577 (1986); ——— and R. M. Soneira, *Astrophys. J. Suppl.* **44**, 73 (1980).
8. F. D'Antona and I. Mazziteli, *Astrophys. J.* **296**, 502 (1985); F. D'Antona, *ibid.* **320**, 653 (1987); J. Liebert, *Stellar Evolution, 50th Anniversary Symposium of McDonald Observatory*, D. L. Lambert, Ed. (Astronomical Society of the Pacific, in press).
9. A. Burrows, W. B. Hubbard, J. L. Lunine, *Astrophys. J.* **345**, 939 (1989).
10. B. J. Boyle *et al.*, *Mon. Not. R. Astron. Soc.* **235**, 935 (1988).
11. J. N. Bahcall and D. P. Schneider, in *IAU Symposium 126*, J. E. Grindlay and A. G. K. Phillip, Eds. (Reidel, Boston, 1988), p. 455.
12. J. F. Jarvis and J. A. Tyson, *Astron. J.* **86**, 476 (1981).
13. R. G. Kron, thesis, University of California, Berkeley (1978).
14. H. L. Johnson, *Ann. Rev. Astron. Astrophys.* **4**, 193 (1966).
15. P. Guhathakurta, in preparation.
16. C. A. Gullixson, P. C. Boeshaar, J. A. Tyson, P. Seitzer, in preparation.
17. J. A. Tyson and R. A. Wenk, in preparation; J. A. Tyson, *Astronomical Society of the Pacific Hubble Symposium*, R. G. Kron, Ed., in press.
18. O. Lahav, private communication.

19. We thank O. Lahav, T. Tyson, and R. Wenk for allowing us to use their unpublished data and acknowledge valuable suggestions by J. P. Ostriker, R. Romani, L. Spitzer, E. Turner, and M. Weinberg. We are grateful to J. MacKenty and to the STScI photographic laboratory for expert help in preparing color images of the simulations. J.N.B. is grateful for the hospitality and stimulation of the scientific staff at STScI, where part of this research was performed. The computer staff of the IAS, in particular D. Saxe and D. Bovee, made many hardware and software contributions to the simulations. P.G. is supported by NSF grant PHY86-20266. J.N.B. and D.P.S. are supported in part by NASA grants NAS5-29225 and NAS8-32902.

The Role of Inheritance in Behavior

ROBERT PLOMIN

Inheritance plays a major role in behavior as shown by selection and strain studies for animal behavior and by twin and adoption studies for human behavior. Unlike simple Mendelian characteristics, genetic variance for behavioral dimensions and disorders rarely accounts for more than half of the phenotypic variance, and multiple genes with small effects appear to be involved rather than one or two major genes. Genetic research on behavior will be transformed by techniques of molecular biology that can be used to identify DNA sequences responsible for behavioral variation. However, the importance of nongenetic factors and the multigenetic control of behavior require new strategies to detect DNA markers that account for small amounts of behavioral variation.

BEHAVIOR IS A NEW FRONTIER FOR MOLECULAR BIOLOGY. IT is the most complex phenotype that can be studied because behavior reflects the functioning of the whole organism and because it is dynamic and changes in response to the environment. Indeed, behavior is in the vanguard of evolution for these very reasons. Genetic analysis of behavioral dimensions and disorders is especially difficult for three additional reasons. First, unlike characteristics that Mendel studied in the edible pea such as smooth versus wrinkled seeds, most behaviors and behavioral problems are not distributed in "either/or" dichotomies—we are not either smooth or wrinkled, psychologically. Second, unlike classic Mendelian disorders such as Huntington's disease that are caused by a single gene with little effect from other genes or environmental background, most behavioral traits appear to be influenced by many genes, each

The author is professor of human development in the Center for Developmental and Health Genetics, College of Health and Human Development, Pennsylvania State University, University Park, PA 16802.